Data Assimilation for POD Reduced-Order Model – Comparison of PF and EnKF

Ryota Kikuchi
Institute of Fluid Science
Tohoku University
Sendai, Miyagi, Japan
rkikuchi@edge.ifs.tohoku.ac.jp

Takashi Misaka
Institute of Fluid Science
Tohoku University
Sendai, Miyagi, Japan
misaka@edge.ifs.tohoku.ac.jp

Shigeru Obayashi
Institute of Fluid Science
Tohoku University
Sendai, Miyagi, Japan
obayashi@ifs.tohoku.ac.jp

An integrated method of a proper orthogonal decomposition (POD) based reduced-order model (ROM) and data assimilation is proposed for real-time prediction of an unsteady flow field. In this paper, a particle filter (PF) and an ensemble Kalman filter (EnKF) are employed for data assimilation and the difference of predicted flow fields is evaluated in detail. The proposed method is validated using identical twin experiments of an unsteady flow field around a circular cylinder at Reynolds number of 1000. The PF and EnKF are employed to estimate coefficients of the ROM based on observed velocity components in the wake of the circular cylinder. The proposed method reproduces the unsteady flow field several orders faster than the reference numerical simulation based on Navier-Stokes equations. Furthermore, the prediction accuracy of ROM-PF is significantly better than that of ROM-EnKF. It is due to the flexibility of PF for representing a predictive probability density function compared to EnKF.

Keywords; Proper Orthogonal Decomposition, Reduced-Order Model, Data Assimilation, Circular Cylinder

I. INTRODUCTION

Atmospheric turbulence poses a potential risk to aircraft operation, therefore, its prediction is important for aviation safety [1]. Numerical weather prediction (NWP) has become an essential tool for aircraft operations. NWP is able to predict weather conditions in synoptic scale and mesoscale. However, it is difficult to reproduce the atmospheric turbulence that is not explicitly represented in NWP. For turbulent wind analysis, large eddy simulation (LES) is commonly used [2]. However, LES requires massive computational resources, therefore, it is not a practical tool for forecasting the atmospheric turbulence.

The possibility to approximate unsteady flows at low computational cost by the reduced order model (ROM) based on the proper orthogonal decomposition (POD) has gained attention. POD is also known as statistical recognition tools [3] or post-processing tools in experiments, i.e., particle image velocimetry [4]. POD is a technique for decomposing a coherent structure into a set of POD basis vectors and eigenvalues. Moreover, they can be used to create a ROM of a flow field. ROM expresses the entire flow dynamics by a system of ordinary differential equations which has much lower dimensions than the original model [5,6]. However, the original ROM may be barely accurate and even unstable in the unsteady flows. One of the main reasons is the truncation of low energy modes in the POD basis vectors [5]. Therefore, there has been extensive research regarding the calibration method for suppressing the computational instability [5,6]. Unfortunately, these methods do not always guarantee the removal of the ROM instability. Furthermore, it is difficult to conduct long time integration only using ROM.

Data assimilation is conducted to reduce the uncertainty of a numerical model by assimilating observation into the simulation. A variety of approaches have been applied in the field of meteorological and oceanic researches [7], because it can determine unknown inputs such as the boundary and initial conditions and other parameters by assimilating observation. There are two types of data assimilation, which are variational and sequential methods. The objective of the variational data assimilation method is to find the solution of a numerical model which will best fit a series of observations distributed over some space and time interval [7]. Sequential data assimilation is able to update the estimation of the simulation at each observation time [8,9].

The integrated method of ROM and data assimilation was addressed for estimating a complex flow field [10]. This study suggested a possibility of the real-time prediction of a unsteady flow field, however, a difference of estimating performance depending on data assimilation techniques was not assessed so far. In the present paper, a particle filter (PF) [8] and an ensemble Kalman filter (EnKF) [9] are applied for data assimilation. PF and EnKF are used to compensate the uncertainty of ROM (ROM-PF, ROM-EnKF). These methods have been used in a wide variety of industrial areas such as image tracking [11]. The uncertain parameters of ROM are updated sequentially by assimilating observations at each observation time. Therefore, it is possible to predict the long-term time evolution of an unsteady flow field with the much lower computational cost than the original model.

We compare the presented methods (ROM-PF and ROM-EnKF) and investigate the effectiveness of the atmospheric turbulence prediction system based on those methods. The actual atmospheric turbulence contains eddies in various scales, however, the limited-size of such eddies can affect the flight of

aircraft. Therefore, it is important to accurately predict a certain scale of the flow field. The numerical experiment is performed by identical twin experiment using the flow field around a circle cylinder for Reynolds number Re = 1000, which is used as test data. The predicted results are compared with the test data to confirm the spatial structure of the von Karman vortex streets.

II. METHOD

A. Numerical Methodology for Fluids

In this study, the Building-Cube Method (BCM) [12] is employed to obtain the flow past a circular cylinder at Re = 1000. BCM is an approach to discretize an entire flow as an assemblage of cubic sub-domains named 'cube.' All cubes have the same number of equally-spaced Cartesian mesh so that the computational load is equally distributed among cubes. This realizes an efficient and simple parallelization of the mesh generation and flow solution processes. The governing equations are the three-dimensional incompressible Navier-Stokes and continuity equations. They can be represented as follows:

$$\frac{\partial \boldsymbol{u}}{\partial t} + (\boldsymbol{u}\cdot\boldsymbol{\nabla})\boldsymbol{u} + \frac{1}{\rho}\nabla p - \frac{\mu}{\rho}\boldsymbol{\nabla}^2\boldsymbol{u} = 0, \qquad \boldsymbol{\nabla}\cdot\boldsymbol{u} = 0, \tag{1}$$

where $\boldsymbol{u}$ represents the three-dimensional wind velocity components (u, v, w), p is the pressure, ρ is the density, and μ is the molecular viscosity. In this study, the convective terms are evaluated by a third-order upwind scheme (Kawamura-Kuwahara scheme) [13]. The viscous terms are evaluated by the second-order central difference. Time integration of the Navier-Stokes equations is performed by the fourth-order Runge-Kutta method. The object surface is represented by the immersed boundary method in order to improve the accuracy of the surface representation [14]. The computational condition and domain are shown in Table 1 and Fig. 1, respectively.

B. POD Reduced-Order Model

The von Karman vortex streets around a circular cylinder for Reynolds number Re = 1000 is simulated by BCM. The model variables $\boldsymbol{u_i}$ is velocity components of a wind velocity field at every step in time t_1, ..., t_k , where K is the number of snapshots that mean the number of calculation steps. The velocity fields $\boldsymbol{u_i}$ are used for snapshot POD [15]. The velocity fields are expressed as the sum of the average component $\overline{\boldsymbol{U}}(x)$ and the fluctuation component. Then, the fluctuations are expanded in terms of the temporal coefficients $a_i(t)$ and the POD basis vectors $\boldsymbol{\Phi}_i(x,t)$ as follows:

$$\boldsymbol{u}(x,t) = \overline{\boldsymbol{U}}(x) + \sum_{i=1}^{r} a_i(t)\boldsymbol{\Phi}_i(x,t), \tag{2}$$

where r is the number of POD modes used in the projection. An important characteristic of these vectors is orthogonality, i.e., $\langle \boldsymbol{\Phi}_i, \boldsymbol{\Phi}_j \rangle$ is equal to δ_{ij} (Dirac delta function). Equation (2) is substituted into incompressible Navier-Stokes equations, projecting these equations onto $\boldsymbol{\Phi}_i$ as follows:

Table 1. Computational conditions.

Number of cube	592
Cells in a cube	16x16x16
Total number of cells	2,424,832
Minimum cell size	0.039
Reynolds number	1000
Time step	0.004

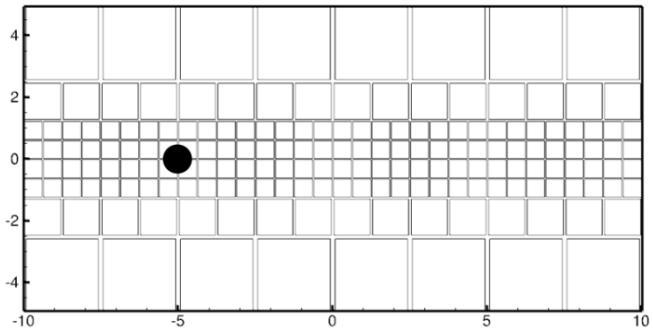

Fig. 1. BCM computational domain for a circular cylinder.

$$\frac{da_i}{dt} = (A_i + \alpha_i) + \sum_{j=1}^{r}(B_{ij} + \beta_{ij})a_j + \sum_{j=1}^{r}\sum_{k=1}^{r} C_{ijk}a_j a_k,$$
$$A_i = -\langle \boldsymbol{\Phi}_i, (\overline{\boldsymbol{U}}\cdot\boldsymbol{\nabla})\overline{\boldsymbol{U}}\rangle + \frac{\mu}{\rho}\langle \boldsymbol{\Phi}_i, \boldsymbol{\nabla}^2\overline{\boldsymbol{U}}\rangle,$$
$$B_{ij} = -\langle \boldsymbol{\Phi}_i, (\boldsymbol{\Phi}_j\cdot\boldsymbol{\nabla})\overline{\boldsymbol{U}}\rangle - \langle \boldsymbol{\Phi}_i, (\overline{\boldsymbol{U}}\cdot\boldsymbol{\nabla})\boldsymbol{\Phi}_j\rangle + \frac{\mu}{\rho}\langle \boldsymbol{\Phi}_i, \boldsymbol{\nabla}^2\boldsymbol{\Phi}_j\rangle, \tag{3}$$
$$C_{ijk} = -\langle \boldsymbol{\Phi}_i, \boldsymbol{\Phi}_j\cdot\boldsymbol{\nabla}\boldsymbol{\Phi}_k\rangle,$$
$$subject\ \ a_i(t_0) = \langle \mathbf{u}(x,t_0) - \overline{\boldsymbol{u}}(x), \boldsymbol{\Phi}_i\rangle.$$

And α_i and β_{ij} are calibration terms. The terms are added to correct the error and instability of original ROM. The obtained a_i represents the time-dependent temporal coefficients of POD. Therefore, unsteady flow field can be obtained with a_i of the POD-Galerkin method and $\boldsymbol{\Phi}_i$ of the snapshot POD. Thus, this approach can reduce massive order of flow calculation.

Although the POD-Galerkin reduced-order model is able to represent unsteady flow fields, the temporal coefficients a_i have a large impact on the representation of the unsteady flow fields. Therefore, data assimilation methods are employed to estimate the temporal coefficients. In the identical twin experiment of data assimilation, the observed velocity components from the reference simulation are used (pseudo observation). In this study, the first to the 30th of POD basis vectors are used for constructing ROM because the sum of the energy from those modes dominates more than 99.9% of the total energy.

C. Data Assimilation

The state space model used for PF and EnKF is given as:

$$\boldsymbol{x}_t = f_t(\boldsymbol{x}_{t-1}, \mathbf{v}_\mathrm{t}), \quad \boldsymbol{y}_t = h_t(\boldsymbol{x}_t, \mathbf{w}_\mathrm{t}), \tag{4}$$

where the vectors $\boldsymbol{x}_t$ and $\boldsymbol{y}_t$ indicate the state vector of a system and observation values at time t, and the vectors $\boldsymbol{v}_t$ and $\boldsymbol{w}_t$ are the system noise and the observation noise. The operator f_t represents the simulation model. h_t is the projection matrix from the simulation space to the observation space. PF and EnKF approximate the probability density functions of each state vectors by a large number of ensemble members, which are termed as 'particles.' An ensemble represents the approximation of probability density functions as follows:

$$p(\boldsymbol{x}_t|\boldsymbol{y}_{1:t-1}) \cong \frac{1}{N}\sum_{i=1}^{N} \delta\left(\boldsymbol{x}_t - \boldsymbol{x}_{t|t-1}^{(i)}\right), \tag{5}$$

where $\left\{\boldsymbol{x}_{t|t-1}^{(i)}\right\}_{i=1}^{N}$ is the ensemble of $\boldsymbol{x}_{t|t-1}^{(i)}$, $\boldsymbol{y}_{1:t} = \{y_1, y_2, \cdots, y_t\}$ represents the observation values, and N is the number of particles. $p(\boldsymbol{x}_t|\boldsymbol{y}_{1:t-1})$ is predictive probability density functions, which is obtained from each particle of the forecast ensemble $\boldsymbol{x}_{t|t-1}^{(i)} = f_t\left(\boldsymbol{x}_{t-1|t-1}^{(i)}, \boldsymbol{v}_t\right)$. The procedure of predictive probability density functions is the same for PF and EnKF.

In the filtering step of PF, the filtered probability density functions $p(\boldsymbol{x}_t|\boldsymbol{y}_{1:t})$ are obtained from the predictive probability density functions $p(\boldsymbol{x}_t|\boldsymbol{y}_{1:t-1})$ is and the observations $\boldsymbol{y}_t$ by using Bayes' theorem as follows:

$$\begin{aligned} p(\boldsymbol{x}_t|\boldsymbol{y}_{1:t}) &= \frac{p(\boldsymbol{x}_t|\boldsymbol{y}_{1:t-1})p(\boldsymbol{y}_t|\boldsymbol{x}_t)}{\int p(\boldsymbol{x}_t|\boldsymbol{y}_{1:t-1})p(\boldsymbol{y}_t|\boldsymbol{x}_t)d\boldsymbol{x}_t} \\ &= \sum_{\mathrm{i}=1}^{N} \omega_\mathrm{i}\, \delta\left(\boldsymbol{x}_t - \boldsymbol{x}_{t|t-1}^{(i)}\right), \end{aligned} \tag{6}$$

where $p\left(\boldsymbol{y}_t\middle|\boldsymbol{x}_{t|t-1}^{(j)}\right)$ is the likelihood of under the observations $\boldsymbol{y}_t$. ω_i is the weight defined as:

$$\omega_i = \frac{p\left(\boldsymbol{y}_t\middle|\boldsymbol{x}_{t|t-1}^{(j)}\right)}{\sum_\mathrm{j} p\left(\boldsymbol{y}_t\middle|\boldsymbol{x}_{t|t-1}^{(j)}\right)}. \tag{7}$$

Their filtered particles $\boldsymbol{x}_{t|t}^{(j)}$ are obtained by resampling the predictive particles $\boldsymbol{x}_{t|t-1}^{(j)}$ with a weight of ω_i of each particle. The filtered particles may contain multiple copies of the predictive particles $\boldsymbol{x}_{t|t-1}^{(j)}$, and some predictive particles are abandoned. The number of copies m_i satisfies

$$m_\mathrm{i} \approx N\omega_\mathrm{i} \tag{8}$$

Thus, the filtered probability density functions $p(\boldsymbol{x}_t|\boldsymbol{y}_{1:t})$ are approximated as

$$\begin{aligned} p(\boldsymbol{x}_t|\boldsymbol{y}_{1:t}) &\cong \sum_{i=1}^{N} \omega_\mathrm{i}\, \delta\left(\boldsymbol{x}_t - \boldsymbol{x}_{t|t-1}^{(i)}\right) \\ &\cong \sum_{i=1}^{N} \frac{m_i}{N} \delta\left(\boldsymbol{x}_t - \boldsymbol{x}_{t|t-1}^{(i)}\right) \\ &= \frac{1}{N}\sum_{i=1}^{N} \delta\left(\boldsymbol{x}_t - \boldsymbol{x}_{t|t}^{(i)}\right). \end{aligned} \tag{9}$$

The filtering step of EnKF procedure is as follows. First, deviation components $\breve{x}_{t|t-1}^{(i)}$ and covariance matrix $\hat{V}_{t|t-1}$ are calculated:

$$\begin{aligned} \breve{x}_{t|t-1}^{(i)} &= x_{t|t-1}^{(i)} - \frac{1}{N}\sum_{i=1}^{N} x_{t|t-1}^{(i)}, \\ \hat{V}_{t|t-1} &= \frac{1}{N-1}\sum_{i=1}^{N} \breve{x}_{t|t-1}^{(i)} \breve{x}_{t|t-1}^{(j)\prime}. \end{aligned} \tag{10}$$

Second, Kalman gain $\hat{K}_t$ is calculated from covariance matrix $\hat{V}_{t|t-1}$ as follow:

$$\hat{K}_t = \hat{V}_{t|t-1} H_t' \left(H_t \hat{V}_{t|t-1} H_t' + \hat{R}_t\right)^{-1}, \tag{11}$$

where H_t represents observation matrix, and $\hat{R}_t$ are the covariance matrix of $\mathbf{w}_\mathrm{t}$. Finally, the filtered ensemble $\boldsymbol{x}_{t|t}^{(j)}$ is obtained by the update equation of the Kalman filtering.

$$x_{t|t}^{(i)} = x_{t|t-1}^{(i)} + \hat{K}_t\left(y_t + \hat{w}_t^{(i)} - H_t x_{t|t-1}^{(i)}\right) \tag{12}$$

D. Identical Twin Experiment

Effectiveness of ROM-PF and ROM-EnKF is investigated by a numerical experiment with pseudo observations, so-called `identical twin experiment.' The experimental method for validation is known in the data assimilation field. At first, BCM is run and the results are applied to the snapshot POD to construct ROM. Next, another result used for the snapshot POD are recorded and these consequences are considered true data. The observation data are constructed from the reference flow field, therefore, the predicted flow fields by ROM-PF and ROM-EnKF can be compared with the reference flow field. In this study, a flow field is defined by the von Karman vortex streets around a circle cylinder for Reynolds number Re = 1000. ROM-PF and ROM-EnKF have necessarily parameters which are related to the simulation and the observation. In this study, a parameter study is conducted to assess the impact of these parameters and to compare the results of the predictions by ROM-PF and ROM-EnKF.

There are two parameters related to the simulation and observation which are the number of particles and the observation noise, respectively. In this study, the number of particles is varied as 50, 100, 500, 1000, and 2000. Concerning the observation noise, actual observation contains various errors, for example, the error derived from the characteristics of the observation device. Therefore, it is necessary to evaluate the effect of the error at the time of performing ROM-PF and ROM-EnKF. For that purpose, pseudo observations are generated by adding the artificial observation noise which

mimics the error. In this study, the horizontal wind velocity components u and v are extracted from the reference flow field, and white noise is added to the extracted results. Assuming that observation noise w_t obeys a Gaussian distribution with zero mean and a variance σ^2. We consider observation noises with variances of 0, 0.05, 0.1, 0.2, and 0.5. In addition, other parameters for the data assimilation are system noise, the number of observation points and the time interval. These parameters are set to constant values. The variance σ^2 of system noise is set to 0.1, the number of observation points is 9 and the position of the observation points is shown as Fig. 2, and the time interval of the data assimilation is 0.4 second. The each parameters are also shown in Table 2.

III. RESULTS

In this section, we demonstrate the ability of ROM-PF and ROM-EnKF to predict the von Karman vortex streets around a circular cylinder for Reynolds number Re = 1000. At first, we apply snapshot POD of the unsteady flow result obtained from BCM and verify the validity of POD basis vectors and the energy ratio of each mode in terms of the flow visualization and energy ratio ranking. Then we assess the performance by applying the calibration method which compares the original ROM, the calibration ROM and the reference flow field. Next, ROM-PF and ROM-EnKF are applied to the von Karman vortex streets in the standard case and the results are compared with the reference flow field. Finally we conduct the parameter study to evaluate the capability of unsteady flow predictions.

The root mean square error (RMSE) of all spatial information of the ROM-PF, ROM-EnKF and the reference flow field at each time is used to estimate the accuracy of the prediction.

$$\mathrm{RMSE}(t) = \sqrt{\frac{\sum_{\mathrm{j}=1}^{M}\left(\boldsymbol{U}_{\mathrm{ROM,t}}^{\mathrm{j}} - \boldsymbol{U}_{t}^{\mathrm{j}}\right)^{2}}{\mathrm{M}}}, \tag{13}$$

where $\boldsymbol{U}_{\mathrm{ROM,t}}^{\mathrm{j}}$ and $\boldsymbol{U}_{t}^{\mathrm{j}}$ are the vectors containing ROM-PF or ROM-EnKF velocity components and the reference flow field at the grid j, respecitively, M is the total number of grid over the domain.

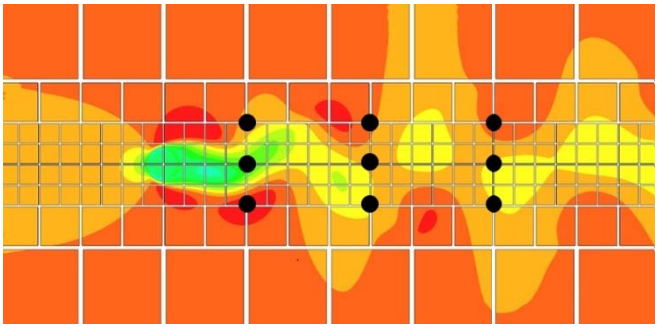

Fig. 2. Location of observed points.

Table 2. Setting of parameter study.

	Parameter setting
Number of particles	50,100,500,1000,2000
Observation noise	0,0.05,0.1,0.2,0.5
System noise	0.1
Number of the observation points	9
Time interval of the data assimilation	0.4

A. *The flow field prediction*

The von Karman vortex streets at Re = 1000 are predicted by ROM-PF and ROM-EnKF in the standard case and the results are compared with the reference flow field. The standard case is defined by the number of particles 500 and the variance of observation noise 0.1. First, the comparison of the spatial characteristic is conducted in Fig. 3. These figures show the color contours of the horizontal wind velocities obtained from using ROM-PF, ROM-EnKF and the reference flow field of BCM, which are from 4 second after the starting time of the flow prediction. As shown in Fig. 3(c) and (d), horizontal velocities of ROM-PF reproduces the von Karman vortex streets. ROM-PF can estimate the frequency and position of the vortices, therefore, the spatial characteristic is reproduced fairly well in comparison to the reference flow field. However, as showed in Fig. 3(e), the stream wise flow velocity of ROM-EnKF loses most of the wind velocity fluctuation which is of interest in the von Karman vortex streets. The cross wise flow velocity of Fig. 3 (f) shows similar but small difference wind velocity fluctuations compared to those of the reference case.

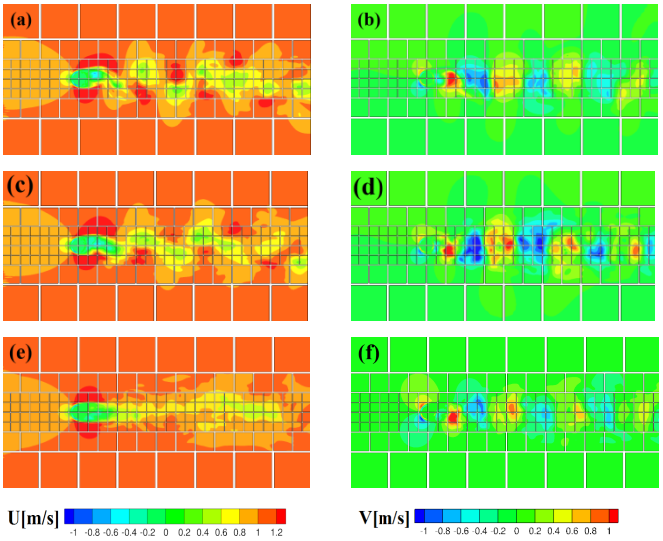

Fig. 3. The result of horizontal velocities of Re =1000, (a), (b): the true obtained from BCM, (c), (d): the result obtained from ROM-PF, (e) and (f) : the result obtained from ROM-EnKF, (a), (c), (e):the stream wise flow velocity at time 4 seconds, (b), (d), (f): the cross wise flow velocity at time 4 seconds.

Next, the time evolutions of the horizontal wind velocities are shown in Fig. 4. These figures show the comparison of the reference flow field obtained from BCM as true value, and the prediction using ROM-PF and ROM-EnKF. In Fig. 4, ROM-PF predicts the time evolution of the reference flow field immediately after the initial is not good even by estimation. The observation used in data assimilation includes the noise, however, it is confirmed that the wind velocity and the frequency can be estimated by filtering the noise from the observation. The results of ROM-EnKF show the major flow structures of the reference flow field, however, the stream wise velocity exhibits the discrepancy from the reference case. In most of the time evolution, the cross wise velocity of ROM-EnKF is smaller than the reference flow field.

Next, the RMSE from ROM-PF and ROM-EnKF are compared with those from the reference case. The RMSE of Re = 1000 during the simulation period is provided in Fig. 5. Each RMSE is large at the beginning but soon decreased and generally stable. In ROM-EnKF, RMSE remains smaller than 0.17 m/s after 10 s, and, the overall average of RMSE is 0.15 m/s. In ROM-PF, RMSE remains smaller than 0.18 m/s after 4 second with an exception at 28 s, where the overall average of RMSE is 0.142 m/s. By comparing the results of ROM-PF and ROM-EnKF, ROM-PF has a larger variation than ROM-EnKF, which can be seen from Fig. 4.

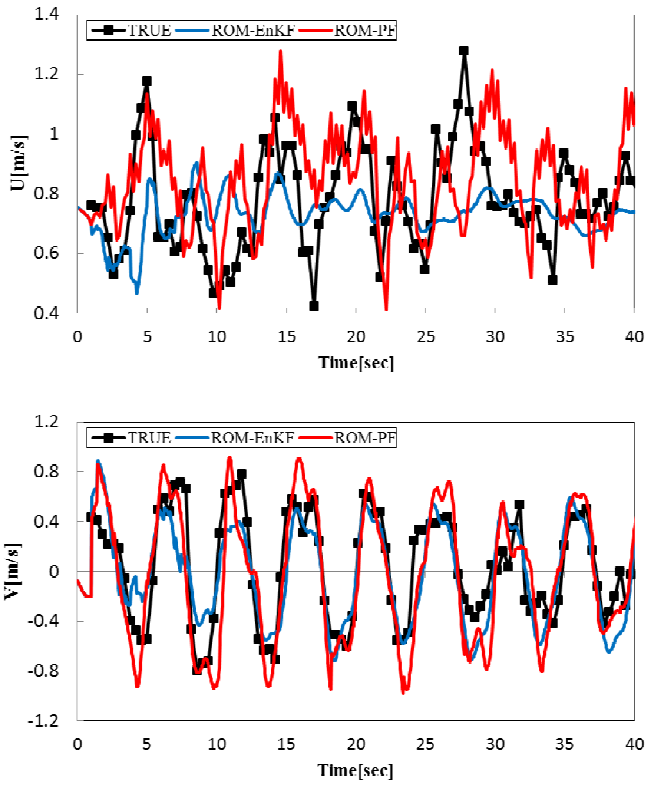

Fig. 4. The time evolution of horizontal velocities, upper figure: the comparison of the stream wise flow velocity; lower figure: the comparison of the cross wise flow velocity.

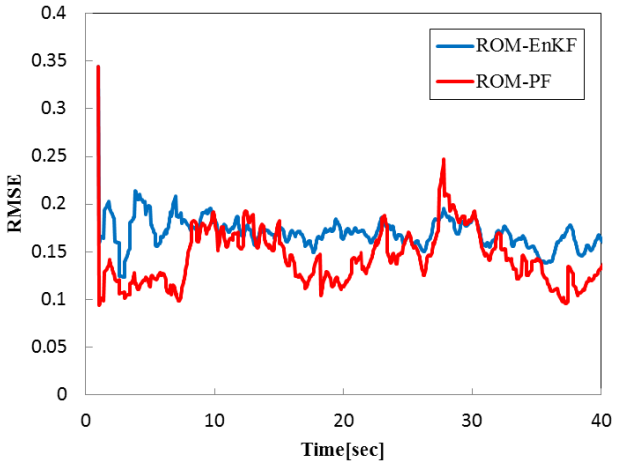

Fig. 5. The time evolution of RMSE.

Finally, the shapes of probability density functions (PDFs) are compared in terms of predictive and filtered PDFs and true value constructed by POD. The PDFs are calculated from the particles concerning the temporal coefficient a_1 at the initial data assimilation step as showed in Fig. 6. The predictive PDF is multimodal distribution, therefore the distribution is significantly different from the Gaussian distribution. In the filtered PDFs of ROM-PF, it is confirmed that the temporal coefficient a_1 which increases the PDFs is near from the true value. In addition, the shape of the PDF remains significantly different from Gaussian distribution. In the filtered PDFs of ROM-EnKF, the peak of the PDFs is far from the true value, and the peak of PDFs that is near from the true value is decreased from the predictive PDF. Furthermore, the shape of PDF is updated to Gaussian-like distribution by EnKF. From the above, when the predictive PDF is far different from the Gaussian distribution, ROM-PF is superior to estimate the flow field, while ROM-EnKF cannot estimate the flow field approperiately.

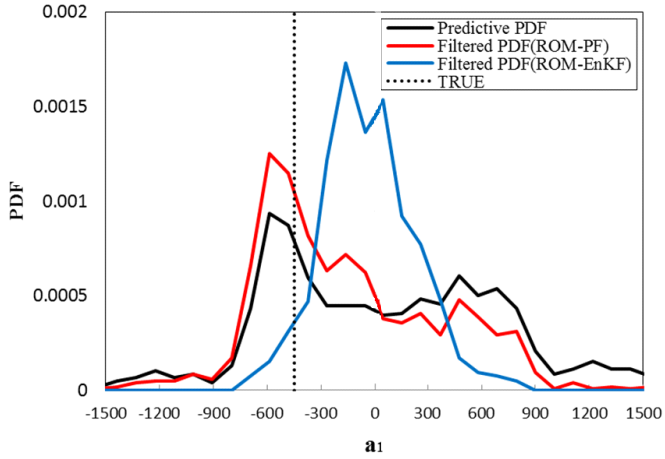

Fig. 6. The probability density functions of a_1 at the initial data assimilation step.

B. *Parameter study for assessment of performance*

ROM-PF and ROM-EnKF are compared in order to identify the effect of the observation noise and the number of particles. Figure 7 represents the plots of overall average RMSE between five different observation noises. First, the effect of the observation noise is investigated by comparing each result in Fig. 7. In both ROM-PF and ROM-EnKF, RMSE reaches a maximum when the variance of observation noise is set to zero. In other cases, it is confirmed that ROM-PF can estimate a lower RMSE than ROM-EnKF. Although ROM-EnKF compares unfavorably, the difference of observation noise has almost no impact on the RMSE.

From the result of the number of particles in Fig. 7 in ROM-PF, it is apparent when the number of the particles is larger, RMSE is smaller. It is possible to ensure the variety of the simulation model by taking a lot of particles. However, the RMSE of ROM-EnKF is not good even by increasing the number of particles. Also, it is found that the retention of the variety is an important concept to predict by ROM-PF in the case of small variation and turbulence.

Computational cost of ROM-PF is largely determined by the number of particles. The result of computational cost is shown in Fig. 8. ROM-PF and ROM-EnKF are calculated by parallel computation with 4 CPUs, and BCM calculation uses 32 CPUs. Figure 8 shows the CPU time which expresses required computational cost for estimation of the flow field for 400 seconds. From the result, as the number of particles increases, the CPU time is increased. ROM-EnKF is slightly higher than ROM-PF, because EnKF needs to the inverse matrix to calculate the Kalman gain. From the result of Fig. 8, the CPU times for ROM-PF and ROM-EnKF are several orders smaller than that of BCM. These results demonstrate the feasibility of predicting an unsteady flow field in real time.

IV. Conclusion

The method for predicting an unsteady flow field in real-time is proposed. The proposed method of reduced order model based on proper orthogonal decomposition and data assimilation is investigated by the identical twin experiments. In this paper, a particle filter (PF) and an ensemble Kalman filter (EnKF) are employed for data assimilation and a difference of estimation performance depending on data assimilation methods is evaluated in detail. The experiments are conducted in the wake of a circular cylinder at Re =1000.

ROM-PF was able to estimate the frequency and position of vortices in the wake of the circular cylinder, therefore, the spatial characteristic was reproduced fairly well in comparison to the reference flow field. However, the stream wise flow velocity of ROM-EnKF loses most of the wind velocity fluctuation which is of interest in the von Karman vortex streets. By comparing ROM-PF and ROM-EnKF, ROM-PF realized a lower RMSE than ROM-EnKF. It is due to the non-Gaussian shape of predictive probability density functions, which could be well handled by PF.

In the parameter study of the observation noise and the number of particles, it was confirmed that ROM-PF was able to estimate a lower RMSE than ROM-EnKF. In ROM-PF, it was apparent when the number of the particles is larger, RMSE is smaller. However, RMSE of ROM-EnKF was not good even by increasing the number of particles. In computational cost, ROM-EnKF was slightly higher than ROM-PF, because EnKF needed to the inverse matrix to calculate the Kalman gain. In addition, the CPU times for ROM-PF and ROM-EnKF were several orders smaller than that of BCM. These results demonstrated the feasibility of prediction the unsteady flow field in real time.

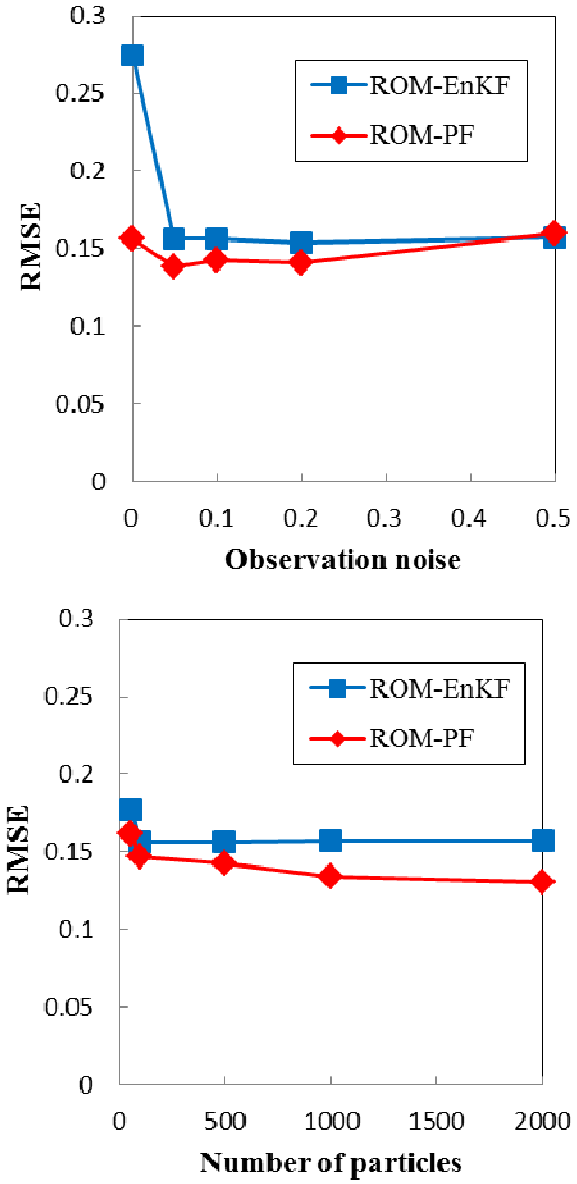

Fig. 7. The parameter study of time average RMSE, upper figure: observation noise; lower figure: number of particles.

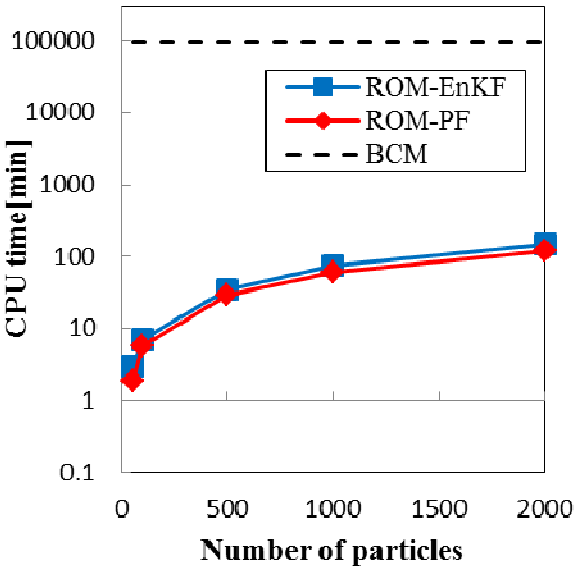

Fig. 8. The computational cost in CPU Time for ROM-PF and ROM-EnKF.

REFERENCES

[1] R. E. Arkell, "Differentiating Between Types of Wind Shear in Aviation Forecasting," National Weather Digest, vol. 24, pp. 39–51, 2000.

[2] C. H. Moeng, J. Dudhia, J. Klemp, and P. Sullivan, "Examining Two-Way Grid Nesting for Large Eddy Simulation of the PBL Using the WRF Model," Monthly Weather Review, vol. 135, pp. 2295–2311, 2007.

[3] A. A. Mohammed, et al., "Human face recognition based on multidimensional PCA and extreme learning machine," Pattern Recognition, vol. 44, pp. 2588–2597, 2011.

[4] N. E. Murray, and L. S. Ukeiley, "An application of Gappy POD," Experiments in Fluids, vol. 42, pp. 79–91, 2007.

[5] M. Couplet, C. Basdevant, and P. Sagaut, "Calibrated reduced-order POD-Galerkin system for fluid flow modeling," Journal of Computational Physics, vol. 207, pp. 192–220, 2005.

[6] V. L. Kalb, and A. E. Deane, "An intrinsic stabilization scheme for proper orthogonal decomposition based low-dimensional models," Physics of Fluids, vol. 19, No.054106, 2007.

[7] K. Saito, et al., "Nonhydrostatic atmospheric models and operational development at JMA," Journal of the Meteorological Society of Japan, vol. 85, pp. 271–304, 2007.

[8] S. Nakano, G. Ueno, and T. Higuchi, "Merging particle filter for sequential data assimilation," Nonlinear Processes in Geophysics, vol. 14, pp. 395–408, 2007.

[9] G. Evensen, "The ensemble Kalman filter: Theoretical formulation and practical implementation," Ocean Dynamics, vol. 53, pp. 343–367, 2003.

[10] R. Kikuchi, T. Misaka, and S. Obayashi, "Estimation of low-level turbulence utilizing the proper orthogonal decomposition and particle filter," 16th International Conference on Information Fusion, pp. 1364-1371, 2013.

[11] R. P. Mahler, "A Theoretical Foundation for the Stein-Winter" Probability Hypothesis Density (PHD)" Multitarget Tracking Approach," Army Reserch Office Alexandria VA, 2000.

[12] K. Nakahashi, and L. S. Kim, "Building-Cube Method for Large-Scale, High Resolution Flow Computations," 42nd AIAA Aerospace Sciences Meeting and Exhibit, AIAA Paper 2004-434, 2004.

[13] T. Kawamura, and K. Kuwahara, "Computation of High Reynolds Number Flow Around a Circular Cylinder with Surface Roughness," 22nd AIAA Aerospace Science Meeting, AIAA Paper 84-0340, 1984.

[14] K. Nakahashi, "Immersed Boundary Method for Compressible Euler Equations in the Building-Cube Method," 20th AIAA Computational Fluid Dynamics Conference, AIAA Paper 2011-3386, 2011.

[15] L. Sirovich, "Turbulence and the dynamics of coherent structures. I-Coherent structures," Quarterly of applied mathematics, vol. 45, pp. 561-571, 2013.